Crispant analysis in zebrafish as a tool for rapid functional screening of disease-causing genes for bone fragility.

Sophie Debaenst[1]; Tamara Jarayseh[1]; Hanna de Saffel[1]; Jan Willem Bek[1]; Matthieu Boone[2], Ivan Josipovic[2], Pierre Kibleur[2], Ronald Young Kwon[3,4], Paul J. Coucke[1]; Andy Willaert[1].

1. Center for Medical Genetics Ghent, Department of Biomolecular Medicine, Ghent University, Ghent, Belgium
2. Center for X-ray Tomography, Department of Physics and Astronomy, Ghent University, Gent, Belgium
3. Department of Orthopaedics and Sports Medicine, University of Washington, Seattle, United States
4. Institute for Stem Cell and Regenerative Medicine, University of Washington, Seattle, United States

Abstract

Heritable Fragile Bone Disorders (FBDs) encompass a spectrum of conditions, from widespread multifactorial to rare monogenic diseases, all characterized by an elevated risk of fractures. The process of validating causative genes and elucidating their pathogenic mechanisms remains a daunting and resource-intensive task. In this study, we evaluated the feasibility of a semi-high throughput zebrafish screening platform for rapid validation and *in vivo* functional testing and validation of candidate disease-causing genes for a wide range of heritable FBDs. Six genes associated with severe recessive forms of Osteogenesis Imperfecta (OI) and four genes associated with bone mineral density (BMD), a key osteoporosis indicator, identified through genome-wide association studies (GWAS) were selected. The crispant screening approach, based on CRISPR/Cas9 technology, was used to phenotype directly in F0 mosaic founder zebrafish. Next-Generation Sequencing (NGS) analysis revealed a mean indel efficiency of 88% across ten different crispants, indicating a high proportion of knock-out alleles and thus resembling stable knock-out models. We applied multiple techniques to evaluate skeletal characteristics at 7, 14 and 90 days post-fertilization (dpf), including microscopy for osteoblast reporter visualization and mineralization by Alizarin Red S staining, and microCT for quantitative skeletal analysis. While larval crispants exhibited variable differences in osteoblast-positive and mineralized surface areas, adult-stage crispants displayed more pronounced and consistent skeletal phenotypes. Notably, all crispants developed malformed neural and haemal arches, with a majority presenting vertebral fractures and fusions, and some showing significant alterations in vertebral bone volume and density. In addition, *aldh7a1* and *mbtps2* crispants experienced increased mortality due to severe skeletal deformities. RT-qPCR analysis of osteoblast differentiation and bone formation markers at larval stages indicated differential expression of osteogenic markers *bglap* and *col1a1a* in a substantial portion of the crispants, hinting at their utility as biomarkers for FBD crispant screening. In summary, our findings demonstrate that crispant screening in zebrafish offers a viable and efficient strategy for the functional assessment of FBD genes. We advocate for a novel comprehensive approach that integrates various techniques and evaluates distinct skeletal and molecular profiles across different developmental and adult stages. This methodology has the potential to provide new insights into the role of these genes in skeletal biology.

Key words: Osteogenesis Imperfecta, osteoporosis, candidate genes, zebrafish model, crispant, skeletal disorders

67 **Introduction**

68 Heritable fragile bone disorders (FBD), which are generally associated with increased fracture
69 risk, range from common multifactorial conditions to rare monogenic diseases (Charoenngam
70 *et al.*, 2023). They present within a wide phenotypic spectrum where monogenic disorders are
71 generally more severe and often include skeletal deformities and extra-skeletal abnormalities.
72 Multifactorial FBD, on the other hand, usually present with milder symptoms that are often
73 restricted to bone fragility. Osteoporosis is a common skeletal disease characterized by low
74 bone mass, low bone mineral density (BMD) and increased fracture risk (Kanis *et al.*, 1994). It
75 affects about 200 million people around the world (Pouresmaeili *et al.*, 2018). In Europe, 5.6%
76 of the population aged over 50 is diagnosed with osteoporosis, making it a highly prevalent
77 disease, especially in the elderly. The risk of osteoporosis is influenced by both environmental
78 factors, such as physical activity, diet preferences, medication use, coexisting diseases, and
79 genetic factors (Ralston and Uitterlinden, 2010). Low BMD and fractures are highly heritable
80 risk factors, with heritability values ranging from 50% to 80% (Brent Richards *et al.*, 2012).
81 Genome-wide association studies (GWAS) in humans have unraveled hundreds of susceptible
82 loci associated with BMD and other bone traits related to risk of osteoporotic fracture (Zhu *et*
83 *al.*, 2021). GWAS results have great potential for the development of drug targets, the
84 identification of risk factors, and risk prediction for osteoporosis. However, the identification
85 of causal genes at these loci or the mechanisms by which GWAS loci alter bone physiology has
86 faced challenges due to the scarcity of *in vivo* validation tools with sufficient throughput (Sabik
87 and Farber, 2017).

88 In monogenic FBD, on the other hand, gene identification is generally more
89 straightforward. One example of such a disease is osteogenesis imperfecta (OI), a genetically
90 heterogeneous connective tissue disorder that is mainly characterized by bone fragility, skeletal
91 deformities, and other extra skeletal manifestations (Forlino and Marini, 2016). Although in the
92 majority of cases, it is caused by autosomal dominant mutations in the collagen type 1 genes,
93 mutations in an increasing number of non-collagen genes causing severe recessive forms of OI,
94 are being identified. These genes encode proteins that are involved in different aspects of bone
95 formation, such as osteoblast differentiation (OSTERIX, WNT1, OASIS, S2P and SPARC),
96 bone mineralization (PEDF and BRIL) and collagen processing (HSP47, FKBP65, LH2,
97 KDELR2, CRTAP, P3H1, CyPB and TRIC-B) (Forlino and Marini, 2016)(Jovanovic *et al.*,
98 2022). Recent sequencing technologies have improved genetic diagnosis, but the investigation
99 of the pathogenesis of the different forms of OI is still a laborious, costly, and time-consuming

100 task. Hence, it is essential to develop efficient and cost-effective methods for *in vivo* functional
101 testing to validate the involvement and mechanistic role of candidate and newly identified
102 causal genes in the pathogenesis of FBD.

103 Zebrafish are a valuable model organism for studying human diseases, as they share a
104 high degree of genetic similarity with humans. More than 70% of human protein-coding genes
105 and 82% of human disease-related genes have zebrafish orthologs, including most of the genes
106 involved in skeletogenesis (Howe *et al.*, 2013). Additionally, zebrafish share many of their
107 skeletal features and ossification mechanisms with mammals (Dietrich *et al.*, 2021) and
108 numerous zebrafish models for skeletal diseases have been established and investigated
109 (Gistelinck *et al.*, 2018)(Daponte *et al.*, 2023)(Kague and Karasik, 2022). These models have
110 some advantages over rodent models, such as longer survival, likely due to the reduced impact
111 of gravity on their fragile skeletons in the aquatic environment, and the availability of transgenic
112 lines marking specific bone cell types combined with the transparency of early life stages
113 allowing for *in vivo* observation of the dynamics of skeletal development (Dietrich *et al.*, 2021).

114 Genome-editing with CRISPR/Cas9 is a fast and easy method to create knockout alleles
115 and stable zebrafish mutant lines (Uribe-Salazar *et al.*, 2022). However, obtaining zebrafish
116 lines that are homozygous for the mutant alleles requires two generations of adult animals (>6
117 months), which limits the efficiency and affordability of genetic screens (Kroll *et al.*, 2021). To
118 overcome these drawbacks, phenotyping the first-generation (F0) mosaic founder zebrafish,
119 also known as crispants, is an emerging approach. Adult crispants have a shorter generation
120 time (~3 months) than stable lines (6 to 9 months), which allows screening more genes in less
121 time and at lower costs and resources. We previously demonstrated the feasibility of this
122 approach by comparing the phenotypes and molecular profiles of a stable knockout line and a
123 crispant for the osteoporosis gene *lrp5*, and found them to be highly similar (Bek *et al.*, 2021).
124 In a study by Watson et al., 2020, comparison of crispants to homozygous germline mutants for
125 *bmp1a* and *plod2*, two causal OI genes, revealed phenotypic convergence, suggesting that
126 crispants faithfully recapitulate the biology of germline skeletal disease models. Therefore,
127 while zebrafish crispant screens are promising as an economic, fast, and biologically relevant
128 genetic screening approach in vertebrate model systems, a rigorous evaluation of their potential
129 to screen for FBD-associated genes is needed.

130 In this study, we aimed to conduct a pilot-study to evaluate the feasibility of zebrafish
131 crispant screening as a gene-based approach for rapid *in vivo* functional screening and
132 validation of a set of causal genes for a broad range of FBD. The selected set includes on one
133 hand genes associated with traits related to osteoporosis which is a relatively mild late-onset

FBD and on the other hand genes causing recessive forms of OI associated with more severe skeletal phenotypes. An overview of the selected genes with observed mutant phenotypes in human, mice and zebrafish is provided in Supplementary Table 1. With this study, we want to provide an experimental platform for medium-sized zebrafish crispant screening of FBD genes.

168 **Results**

169 **Generation of zebrafish crispants for osteoporosis and OI genes**

170 To identify and prioritize potential causal genes for osteoporosis, we used the GWAS
171 catalog (Sollis *et al.*, 2023). We selected the variants associated with bone density and ranked
172 them by their GWAS evidence, i.e., the number of independent publications that reported
173 significant associations. We then identified the genes that harbored these variants and chose the
174 top four candidates with single zebrafish orthologs: *ALDH7A1*, *ESR1*, *DAAM2* and *SOST*.
175 Furthermore, we selected six genes associated with recessive forms of OI associated with severe
176 skeletal phenotypes, and involved in different aspects of bone formation, including osteoblast
177 differentiation (*CREB3L1, MBTPS2 and SPARC),* bone mineralization (*SERPINF1* and *IFITM*)
178 and collagen transport (*SEC24D*).

179 For each of the 10 selected genes and "scrambled" sequence, Alt-R™ gRNAs (IDT)
180 were designed through a thorough procedure, via the Benchling platform. For each gene, the
181 gRNA with the highest out-of-frame (OOF) efficiency, as predicted by the InDelphi-mESC
182 prediction tool (Supplementary Figure 1), was selected for co-injection with Cas9 into one-cell
183 stage embryos. Based on previous studies, we assumed that high indel (insertion/deletion) and
184 OOF efficiencies result in a sufficient reduction or inactivation of the corresponding protein in
185 crispants to induce a skeletal phenotype (Naert *et al.*, 2020). DNA from a pool of 1 dpf larvae
186 (n=10) for the different crispants and corresponding sibling controls, was extracted, and
187 subjected to NGS analysis. Sequencing data was analyzed using the Crispresso2 tool (Clement
188 *et al.*, 2019) to determine the fraction of reads containing indels, the OOF rate and the number
189 of in-frame deletions consisting of more than 6 base pairs in these pools (Table 1).

190 Across the different crispants the minimal indel efficiency was 71%, while the OOF rate
191 ranged between 49 and 73%. We subsequently determined the proportion of reads containing
192 in-frame deletions of at least 6 base pairs, resulting in the removal of 2 or more amino acids
193 (Table 1; Supplementary Figure 1). Such deletions have a relatively high chance of impairing
194 protein function (Emond *et al.*, 2020)(Savino *et al.*, 2022)(Miton and Tokuriki, 2023). The
195 accumulated percentage of reads with indels that likely cause loss-of-function of the respective
196 protein (OOF % + % in-frame indel ≥ 6bp), fall within the range of 60% to 92%, although also
197 reads with short in-frame indels (<6bp) can affect protein function. Finally, we investigated the
198 occurrence of off-target effects in these samples by analyzing NGS data from the three most
199 probable off-target sites per crispant, as determined by the CFD score provided by the
200 CRISPOR tool (Concordet and Haeussler, 2018). In 20 out of the 30 examined off-target sites,

201 no off-target mutations were identified (Supplementary Table 2). For the remaining off-target
202 sites, the off-target rate ranged from 0,11% to 2,82%. This included basepair substitutions
203 which are most likely sequencing errors, or true off-target indel variants, present in such low
204 number of genomes that it is negligible in terms of biological impact in the crispants.

205 **Assessment of the early skeleton in crispants reveals differences in osteoblast-**
206 **positive and mineralized surface areas.**

207 Crispants and sibling controls were raised until 7 or 14 dpf. At this point the presence
208 of immature osteoblasts in the head region was visualized using the transgenic *osx:Kaede*
209 background. Images from 10 larvae per crispant were captured from the ventral perspective at
210 7dpf and from both ventral and lateral perspectives at 14dpf, as this provides a more
211 comprehensive view of the opercle's surface area that can be clearly visualized at that time.
212 The osteoblast-positive areas in both the total head and the opercle were then quantified to gain
213 insight into the formation of new skeletal tissue during early development (Figure 1a;
214 Supplementary Figure 2, 3).

215 At 7 and 14 dpf, *esr1* crispants exhibited a significant increase of the osteoblasts-
216 positive surface area within the head ($p \leq 0,05$; $p \leq 0.001$) (Figure 1b, 1c). Additionally, *ifitm5*
217 crispants at 14 dpf also displayed a significant increase ($p \leq 0.01$) in osteoblasts-positive surface
218 area within the head. Finally, the increased osteoblasts-positive surface area was also observed
219 in the opercle of both crispants at 14 dpf (*esr1* $p \leq 0.001$; *ifitm5* $p \leq 0.01$) and in the opercle of
220 *serpinf1* ($p \leq 0.01$) and *sparc* ($p \leq 0.05$) crispants.

221 Subsequently, Alizarin Red S (ARS) staining was conducted on the same 7 and 14 dpf
222 crispant zebrafish larvae in order to evaluate the degree of mineralization in the early skeletal
223 structures. Ventral views were captured at 7 dpf, while both ventral and lateral views were
224 obtained at 14 dpf. These lateral images at 14 dpf served a dual purpose: they facilitated
225 measurement of the mineralized surface area of the opercle and allowed for quantification of
226 the number of mineralized vertebrae. We quantified the mineralized surface areas of the total
227 head, the notochord tip, and the opercle, as well as determined the number of vertebrae (Figure
228 1a; Supplementary Figure 4, 5).

229 At 7dpf, the total head exhibited a significant reduction in mineralized surface in
230 *aldh7a1* ($p \leq 0.05$) and *sec24d* crispants ($p \leq 0.0001$), while the notochord tip displayed a
231 significant increase in mineralized surface area in *creb3l1* ($p \leq 0.05$), *ifitm5* ($p \leq 0.05$), and
232 *serpinf1* ($p \leq 0.05$) crispants (Figure 1b). At 14 dpf, a similar trend of reduced mineralized
233 surface area of the total head was observed in *aldh7a1* and *sec24d* crispants, albeit not reaching

234 statistical significance. In contrast, the mineral surface are of the head was significantly
235 increased in *esr1* crispants ($p \leq 0.05$). Furthermore, the increased mineralization of the
236 notochord tip remained significant in *ifitm5* crispants ($p \leq 0.01$), while it normalized in *creb3l1*
237 and *sec24d* crispants. A novel increase emerged in *esr1* crispants ($p \leq 0.05$). Finally, at 14 dpf,
238 *sec24d* crispants exhibited a significant decrease ($p \leq 0.001$) in the mineralized surface area of
239 the opercle and the number of mineralized vertebrae, whereas *serpinf1* crispants showed a
240 notable increase in the number of mineralized vertebrae ($p \leq 0.01$) (Figure 1c).
241

242 **RT-qPCR expression analysis reveals differential expression of osteogenic markers**
243 ***bglap* and *col1a1a* in a significant subset of crispants.**

244 To explore the expression level of different osteogenic markers throughout the set of
245 crispants, RT-qPCR analysis was performed on whole larvae at 7 and 14 dpf. At 7dpf, no
246 significant differences were seen in the expression of *runx2*, an early pre-osteoblast marker,
247 between the different crispants and corresponding controls. *Osterix,* also known as *sp7*, a *runx2*
248 downstream gene which plays a critical role for the differentiation of pre-osteoblasts into
249 mature osteoblasts*,* was only upregulated in crispants for *sparc* ($p \leq 0{,}001$). Osteocalcin, also
250 known as *bglap,* which is mainly expressed in mature osteoblasts, was downregulated in almost
251 all crispants, except in crispants for *sost* and *sparc.* Finally, *col1a1a,* encoding the $\alpha 1$ chain of
252 type 1 collagen, and marking extracellular matrix synthesis by both pre- and mature osteoblasts
253 (Valenti *et al.*, 2020), was upregulated in crispants for *aldh7a1* ($p \leq 0{,}001$), *daam2* ($p \leq 0{,}05$),
254 *esr1* ($p \leq 0{,}05$) and *sec24d* ($p \leq 0{,}05$) (Figure 2a).

255 At 14dpf, the expression of *runx2* remained unchanged in all crispants compared to
256 control. The expression of *sp7* was significantly increased in crispants for *daam2* ($p \leq 0{,}05$) and
257 *sec24d* ($p \leq 0{,}05$), decreased in *esr1* crispants, while expression levels were normalized in *sparc*
258 crispants relative to 7 dpf ($p \leq 0{,}05$). The expression of *bglap* remained significantly
259 downregulated in crispants for *aldh7a1* ($p \leq 0{,}001$), *daam2* ($p \leq 0{,}01$), *esr1* ($p \leq 0{,}01$) and
260 *creb3l1* ($p \leq 0{,}05$) while it reverted to control levels in *ifitm5*, *sec24d* and *serpinf1* crispants.
261 An upregulation in the expression of *col1a1a* was seen in all the crispants, except in crispants
262 for sparc and for *aldh7a1* and *esr1* where expression levels normalized compared to 7dpf
263 (Figure 2b).
264

265 **Assessment of the adult skeleton in FBD crispants reveals frequent morphological**
266 **abnormalities and quantitative differences in vertebral bone parameters.**

267 Crispants were further grown into adulthood (90dpf) and subjected to whole-mount
268 ARS staining for mineralized bone, in order to identify skeletal abnormalities. Crispants for
269 both *aldh7a1* and *mbtps2* displayed early lethality. Survival analysis indicated that *aldh7a1*
270 crispants experienced increased lethality from 7dpf onwards, with no survivors beyond 20dpf,
271 while *mbtps2* crispants exhibited increased lethality from 17dpf onwards, with only a very small
272 number of fish surviving into adulthood (90dpf) (Figure 3). ARS staining of the skeleton of two
273 surviving adult *mbtps2* crispant fish revealed severe cranial malformations, including
274 underdevelopment of the premaxilla, dentary, and articular. However, the vertebral column
275 seemed to be only mildly affected.
276 Among the eight crispants that successfully matured into adulthood, none exhibited
277 significant differences in standard length and head size (n=5 fish per crispant) (Figure 4b).
278 However, *esr1* crispants were observed to have notably larger eye diameters (Figure 4b). All
279 these crispants demonstrated various abnormalities in the caudal part of the vertebral column
280 such as fusions, compressions, fractures, or arch malformations, except for *daam2* crispants
281 where no obvious abnormalities were detected (Figure 4a,c; Supplementary Figure 6). In
282 *creb3l1* crispants the vertebral phenotype was relatively mild and primarily restricted to arch
283 malformations.
284 Next, the adult skeleton of the different crispants and sibling controls was visualized
285 by microCT scanning and the data was quantified and further analyzed using FishCuT software
286 (Hur *et al.*, 2017). For each of the vertebral centra, the length, tissue mineral density (TMD),
287 volume, and thickness were determined and tested for statistical differences between groups
288 using a regression-based statistical test (Supplementary Figure 7). To quantify the extent of
289 differences between crispants and their controls, the means of these parameters in the crispants'
290 vertebral column, were normalized to the standard deviation of the controls, resulting in a z-
291 score [z-score = (mean crispant – mean control) / SD control] (Gistelinck et al., 2018). A
292 significant increase in centrum volume was observed in *daam2* crispants compared to the
293 controls ($p < 0.05$, $z= 2.86$) (Figure 4d). Centrum TMD was significantly higher, and to a similar
294 extent, in crispants for *daam2* ($p < 0.05$; $z= 1.54$) , *esr1* ($p < 0.05$; $z= 1.62$), and *sost* ($p < 0.05$;
295 $z= 1.41$), three genes likely involved in osteoporosis pathogenesis. Centrum thickness was
296 increased in crispants for *esr1* ($p <0.05$; $z= 4.26$), *ifitm5* ($p < 0.01$; $z= 7.13$), and *sec24d* ($p <$
297 0.05; $z= 5.04$) with the most pronounced increase observed in *ifitm5* crispants. Centrum length
298 was increased only in *daam2* crispants ($p < 0.05$; $z= 4.22$).
299

300 **Discussion**

301 The generation of a diverse array of null alleles through CRISPR/Cas9-induced F0 mosaic
302 (crispant) zebrafish offers specific advantages compared to stable knockout zebrafish lines, in
303 particular for rapid screening of phenotypes (Naert *et al.*, 2020). In this study we tested the
304 efficacy of a semi-high throughput zebrafish crispant analysis for rapid validation of candidate
305 disease causing genes for skeletal disorders across a broad phenotypic spectrum. On one hand
306 we included genes for non-classical recessive OI, which is an early-onset monogenic skeletal
307 syndrome with severe skeletal deformities. On the other hand, we screened a set of top
308 candidate genes for osteoporosis, which is a rather late-onset multifactorial disease with little
309 to no deformities. All selected genes show skeletal expression in both human and zebrafish. An
310 overview of the selected genes with observed mutant phenotypes in human, mice and zebrafish
311 is provided in Supplementary Table 1. It is important to note that this study focused on
312 candidate genes for osteoporosis, not on the role of specific variants identified in GWAS
313 studies. Non-coding variants for instance, which are often identified in GWAS studies, present
314 significant challenges in terms of functional validation and interpretation. In this study we
315 propose a crispant screening platform that combines various phenotypic and molecular assays
316 at three key developmental and adult stages (7, 14 and 90 dpf). To obtain a general overview
317 of the results for the selected crispants, all results were summarized in Table 2.

318 At two distinct larval stages, 7 dpf and 14 dpf, diverse measurements of the early
319 skeleton were conducted, including an assessment of both the osteoblast-positive and the
320 mineralized surface areas located in the head region. The osteoblast-positive area represents the
321 quantity of osteoblasts within a given structure and is a measure of the formation of bone matrix.
322 Although a general tendency towards increased areas could be noted across different crispants
323 at 14dpf, only crispants for *esr1* showed a consistent increase at both 7 and 14 dpf. Interestingly,
324 Brett et al., 2021 extensively investigated *esr1* mutations in the context of hormone receptor-
325 positive breast cancer but did not evaluate the presence of osteoblasts. However, the depletion
326 of estrogen in an osteoblastic cell line *in vitro* results in the stimulation of osteoblast
327 differentiation (Schiavi *et al.*, 2021).

328 The extent of mineralization of the head skeletal elements was found to be mostly not
329 different compared to controls, although in the crispants where significant differences were
330 detected at one of the studied time points, the mineralization of the head skeleton elements was
331 mostly lower and of the notochord tip higher. Only crispants for *sec24d*, a gene critical for
332 transporting extracellular matrix (ECM) proteins, exhibited reduced mineralization in different

head structures both at 7dpf and 14dpf. These findings aligned with the observed malformations in *bulldog* zebrafish, where disrupted *sec24d* function leads to head abnormalities and growth delays in early larval stages (Sarmah *et al.*, 2010). Although the measurements of osteoblast-positive and mineralized surface areas may be influenced by size differences among some of the crispants, normalization to size parameters was not conducted, as variations in growth were considered integral to the phenotypic outcome.

Despite considerable variability in the measurements we conducted, a subtle trend emerged in the expression data for osteogenic markers during early stages. Specifically, the expression of *bglap*, a late osteoblast differentiation marker appeared to be consistently downregulated in near all crispants, except for crispants for *sost*, *mbtps2* and *sparc* at 7 dpf. However, this downregulation became less pronounced at 14 dpf, affecting only crispants for *aldh7a1, daam2, esr1* and *creb3l1.* Interestingly, most crispants for genes involved in the pathogenesis of osteoporosis exhibited this downregulation, except for *sost*, where the expression of *bglap* remained unaffected. In contrast, the expression of *col1a1a* showed an opposing trend. Initially, a modest upregulation of this marker was observed at 7 dpf, limited to just four crispants. However, this effect intensified over time, with nearly all crispants displaying upregulation at 14 dpf, except for *aldh7a1*, *esr1*, and *sparc*. The remarkable upregulation of *col1a1* expression could potentially arise from an abundance of immature osteoblasts within the cranial skeleton, a phenomenon we frequently observed across the set of crispants (Amarasekara *et al.*, 2021). These osteoblasts play an active role in the synthesis of the organic bone matrix, including the production of collagen type I fibers. Interestingly, the generally diminished expression of the late osteoblastic marker *bglap* corroborates the presence of less mature osteoblasts (Gavaia *et al.*, 2006). As mainly mature osteoblasts engage in the deposition of calcium and phosphate ions, essential for the formation of hydroxyapatite crystals, bone mineralization can be expected to be reduced in the crispants, which results in increased formation of non-mineralized osteoid deposits. Indeed, we observed that despite often increased bone osteoblast-positive surfaces, mineralization-positive areas in the head skeleton were frequently found to be reduced (Salhotra *et al.*, 2020). The differential expression profiles of the osteogenic markers *bglap* and *col1a1a* highlight their potential as biomarkers for osteoblast differentiation and bone formation in FBD crispant screens. However, it is important to note that the genes evaluated by RT-PCR are not exclusively expressed in bone tissue. Since whole-body samples were used for expression analysis, there is a possibility that the observed changes in gene expression may be influenced by other non-skeletal cell types.

366 In early stages of development, we observed that crispants, although presenting with a
367 high indel frequency, showed a relatively high variability for the phenotypic parameters we
368 tested (mineralization and osteoblast surface areas), which often prevented reaching statistical
369 significance. Phenotypic variability in these zebrafish larvae can be attributed to several factors,
370 including crispant mosaicism, allele heterogeneity, environmental factors, differences in
371 genomic background and development, maternally-deposited RNAs, and slightly variable
372 imaging positioning. In our study, for each crispant and corresponding controls, all experiments
373 at different ages were conducted on zebrafish from the same clutch, allowing analysis of a
374 developmental time series in animals with a relative genetically homogeneous background.
375 Although increasing the number of biological replicates could potentially enhance statistical
376 power, previous studies have not confirmed this (Winter *et al*., 2022). Enhancing out-of frame
377 (OOF) rates by simultaneously targeting a single gene with multiple crRNAs could potentially
378 increase the penetrance of phenotypic abnormalities observed in early crispants. By directing
379 crRNAs to multiple loci within one gene, the likelihood of introducing frameshift mutations
380 increases significantly. This is suggested to lead to a higher rate of biallelic knockout and reduce
381 the chances of retaining the functional protein (Kroll *et al.*, 2021). However, this also elevates
382 the likelihood of off-target effects, increases double-strand breaks and toxicity, while
383 simultaneously increasing costs (Wu *et al.*, 2018). Furthermore, also in-frame indels affecting
384 two or more amino acids, detected in a substantial proportion of NGS reads in our study, are
385 likely to have a detrimental effect on protein function (Emond *et al.*, 2020)(Savino *et al.*,
386 2022)(Miton and Tokuriki, 2023). Therefore, and because we used highly efficient two-part
387 guide RNAs (Alt-R™ CRISPR-Cas9 system, we opted for single crRNA injections. While there
388 remains a possibility of false negatives, the overall indel efficiency, as indicated by our NGS
389 analysis, is high (>90%), thereby reducing the likelihood of having crispants with very low
390 indel efficiency.
391 In adult crispants, the skeletal phenotype was generally more penetrant. All crispants
392 showed malformed arches, a majority displayed vertebral fractures and fusions and some
393 crispants exhibited distinct quantitative variations in vertebral body measurements.
394 Additionally, these skeletal malformations were consistently observed in a second clutch of
395 crispants (Supplementary Figure 8), underscoring the reproducibility of these phenotypic
396 features across independent clutches. This confirmed the role of the selected genes in skeletal
397 development and homeostasis and their involvement in skeletal disease and established the
398 crispant approach as a valid approach for rapidly providing *in vivo* gene function data to support
399 candidate gene identification.

400 Osteoporosis is typically linked with symptoms that appear late in life. However, our results
401 challenged this notion, by showing that in crispants for osteoporosis genes, skeletal
402 abnormalities can manifest earlier and are not solely reflected in changes to bone mineral
403 density (BMD). For instance, we found that *aldh7a1* and *esr1* crispants displayed significant
404 skeletal anomalies already at larval stages, with *aldh7a1* crispants showing early lethality. At
405 adult stages, *esr1* and *sost* crispants demonstrated various morphological abnormalities of the
406 vertebral column such as fusions, compressions, and arch malformations. The more pronounced
407 and earlier phenotypes in these zebrafish crispants are most likely attributed to the quasi knock-
408 out state of the studied genes, while more common less impactful variants in the same genes
409 result in typical late-onset osteoporosis (Laine *et al.*, 2013) . This phenomenon is also observed
410 in knock-out mouse models for these genes (Melville *et al.*, 2014)(Coughlin *et al.*, 2019).
411 Interestingly, all adult crispants for osteoporosis genes demonstrated a substantial increase
412 in centrum Tissue Mineral Density (TMD). TMD is quantitative measure of the actual mineral
413 volume within bone tissue, computed as bone mineral content over the bone volume
414 (mgHA/cm3) and obtained through mCT or pQCT. In human patients, reduced bone mineral
415 density (aBMD), a measure for the bone mineral content in a projected bone area and assessed
416 using dual energy X-ray absorptiometry (DXA), is frequently linked to osteoporosis. However,
417 also TMD, or vBMD, can be evaluated in the trabecular and cortical bone. Knock-out mice
418 lacking Sost showed an increase in TMD within the cortical bone, which is comparable to the
419 bone present in the zebrafish vertebral column (Li *et al.*, 2008). As for the other genes, for
420 *daam2*, mutant mice with a hypomorphic *Daam2* allele presented with reduced bone strength
421 and increased cortical bone porosity (Morris *et al.*, 2019). *ERα* knockout mice presented with
422 a decrease in cortical bone mineral density and increase in trabecular bone mineral density
423 (Melville *et al.*, 2014). Further studies are needed to better understand how high TMD values
424 observed in these crispants relate to phenotypic changes observed in these mouse models.
425 Finally, it is worthwhile to note that, osteoporosis typically correlates with low vBMD values.
426 While neither the causal variant nor the biological direction of its effects on the target gene are
427 known for BMD-associated loci harboring these genes, the increased TMD following gene
428 knockdown in our models may help to assign the directionality of their effects, and puts forth
429 the possibility that variants at these loci alter the expression of genes that converge on a
430 common biological process that in zebrafish, when disrupted results in the high TMD.
431 Conversely, crispants for genes involved in recessive forms of OI, an early-onset severe
432 skeletal disorder, can intuitively be expected to exhibit pronounced skeletal abnormalities
433 already in larval stages. Interestingly, during these early stages, the majority of the crispants do

434 not exhibit consistent skeletal abnormalities. Although this could be partially explained by the
435 above-discussed variability of the phenotypic outcomes we measured, also human OI subjects
436 with these severe conditions, often experience disease onset during infancy only, with
437 progressive worsening of the skeletal phenotype (Selina *et al.*, 2023).

438 The phenomenon of genetic compensation could play a role in explaining why early
439 phenotypes manifest differently in human patients compared to zebrafish. Genetic
440 compensation ensures an organism to maintain its genetic robustness, even when genetic
441 variation, possibly induced by mutations, occurs. This compensation mechanism can be
442 triggered by the upregulation of compensating genes, often mediated through the regulation of
443 nonsense-mediated decay (NMD) in combination with the epigenetic machinery in zebrafish
444 (El-Brolosy Mohamed A. and Stainier, 2017) (Jakutis and Stainier, 2021). Crispants, in contrast
445 to morphants, also undergo NMD although in a mosaic manner. In larval crispant,
446 compensatory mechanisms may effectively mask the impact of gene loss. However, in adult
447 crispants, the cumulative effect of this loss becomes more pronounced, leading to a later onset
448 phenotype. Furthermore, specific tissues or cell types within the organism may activate
449 compensatory pathways more efficiently, thereby influencing the overall manifestation of the
450 phenotype. When a gene is disrupted in humans, the consequences can be more severe due to
451 the complexity of human development and biology. Such disruptions may result in
452 developmental abnormalities, leading to an early onset of phenotypic traits (Rouf *et al.*, 2023).

453 To conclude, our study proposes a multifaceted gene-based approach to investigate
454 zebrafish crispants associated with heritable FBDs, employing various techniques, and
455 assessing different skeletal phenotypes and molecular profiles at distinct developmental stages.
456 While this work represents a pioneering effort in establishing a screening platform for skeletal
457 diseases, it offers opportunities for future improvement and refinement. For instance, analyzing
458 different skeletal structures and cell types within various transgenic lines, increasing sample
459 size, and incorporating a broader range of techniques, such as phenotypic scoring based on the
460 type of malformations seen in the vertebral column or alcian blue staining for cartilage tissue
461 evaluation, could enhance the comprehensiveness of the screening process and the skeletal
462 phenotype. Moreover, to explore the underlying mechanisms contributing to disease
463 phenotypes, it is essential to establish stable knockout mutants derived from the crispants.
464 Nonetheless, our initial set-up demonstrates the feasibility of this approach to identify genes
465 potentially implicated in the pathogenesis of skeletal disorders, as all studied crispants exhibit
466 skeletal abnormalities in adult stages. These findings support the prospect of crispant screening

467 as a promising tool for rapid functional assessment of candidate genes for skeletal disorders,
468 providing valuable insights into the roles of these genes in skeletal biology.
469

470 # Materials and methods

471 ## Zebrafish maintenance and breeding

472 The zebrafish were incubated at 28°C until 5 days post-fertilization (dpf). Then, they
473 were reared in a rotifer/zebrafish polyculture system from 5dpf to 9dpf following the method
474 of Lawrence et al., 2016. After 10dpf, they were transferred to 3.5 liter tanks in the Core
475 Zebrafish Facility Ghent (ZFG) and housed in semi-closed recirculating systems (Tecniplast).
476 The water parameters were maintained at 27°C, pH 7.5, conductivity 550 µS, and a 14/10
477 light/dark cycle. The zebrafish were fed with Zebrafeed (Sparos) and Gemma Micro dry food
478 (Inve) in the morning and Micro Artemia (Ocean Nutrition) in the afternoon. The *osx*:Kaede
479 transgenic line was used for all experiments. Breeding and embryo collection were done
480 according to standard protocols (Westerfield, 2000). All animal studies complied with EU
481 Directive 2010/63/EU for animals, permit no. ECD 23/27 (Ghent University). Pain, distress,
482 and discomfort were minimized as much as possible.

483 ## Generation of crispants through CRISPR/Cas9 genome editing

484 *Guide RNA design*

485 For the generation of crispants we largely followed the methods described in Bek et al.
486 (2021). In summary, two-part guide RNAs (gRNAs) were used which are functional gRNA
487 duplexes made of a universal 67 mer trans-activating CRISPR-RNA (tracrRNA) and a target-
488 specific CRISPR-RNA (crRNA) (Alt-R™ CRISPR-Cas9 System, IDT). A non-specific crRNA
489 (GCAGGCAAAGAATCCCTGCC), referred to as the 'scrambled' sequence, was used to
490 generate the controls (Wu *et al.*, 2018).

491 The crRNAs corresponding to the genes of interest were designed with the web-based
492 tool Benchling (https://benchling.com), using GRCz11 as a reference genome. With this tool,
493 20 bp crRNAs target sequences, that are followed by a 'NGG' PAM sequence, were listed.
494 Further selection was based on a few specific criteria to minimize the risk of producing
495 (partially) active truncated protein products and potential off-target effects. Specifically,
496 crRNA target sequences located in exon 1, in the last exon, within the last 55bp of the second-

497 to-last exon or in exons consisting of (n) x 3 bp were excluded. Additionally, crRNAs with the
498 highest possible scores for both on-target (Doench *et al.*, 2016) and off-target (Hsu *et al.*,
499 2013)were selected.

500 For the selected crRNA sequences, the Indelphi tool
501 (https://indelphi.giffordlab.mit.edu) employing the mESC training set, was used to predict the
502 DNA repair outcomes (mixture of indels) resulting from non-homologous end-joining (NHEJ)
503 and microhomology-mediated end-joining (MMEJ) induced by CRISPR/Cas9 cleavage. The
504 crRNAs that were predicted to result in high percentages of out-of-frame indels and a limited
505 number of possible genotypes (high precision) were prioritized.

506 Eventually, 1 crRNA per gene was ordered from IDT (https://www.idtdna.com):
507 *aldh7a1* (AATTGTTCGACAGATTGGAG), *daam2* (GATCTATTGCAGTAAGAAGA), *esr1*
508 (GCTCACGACAGAAACACAGC), *sost* (CTGCTCACTCCCGCACCCAG), *creb3l1*
509 (ACACAGTTACTCTCTCAGCG), *ifitm5* (AGCGCAGGAATGCTCAGACA), *mbtps2*
510 (TTCCATATCAAGTGGCACAC), *sec24d* (GCCTATGGATCTCCAACACA), *serpinf1*
511 (CAGGTTGTAGCCAAAATCAG), *sparc* (AGAGGAGCCAGCTGTTGAAG).

512 To predict the potential off-target effects of the selected crRNAs, Crispor
513 (http://crispor.tefor.net) was used. The cutting frequently determination (CFD) off-target score
514 was used to predict the probability of off-target cleavage. The three targets with the highest
515 CFD scores were selected and PCR-amplified (Supplementary Table 2). Next-generation
516 sequencing using the Miseq platform was used to assess the frequency of the off-target effects
517 (Concordet and Haeussler, 2018).

518 *Injection*

519 To prepare gRNA duplexes for each assay, we mixed 200µM crRNA and 200µM
520 tracrRNA, heated the mixture at 95°C for 5 minutes, and then cooled it to room temperature.
521 Next, we micro-injected one-cell-stage Tg(osx:Kaede) zebrafish embryos. The injection mix
522 consisted of a 1.4 nL drop containing RNase-free water, KCl (2000 mM) and
523 ribonucleoproteins (RNPs), consisting of 800 pg of both gRNA duplex and Cas9 (1000 ng/µl)
524 (ToolGen, Seoul, South Korea; wild-type nuclease with nuclear localization signal) protein. For
525 each crispant and each corresponding control, a total of 200 eggs, originating from the same
526 clutch, were injected.

527 **Next-generation sequencing analysis**

528 We extracted DNA from 10 pooled embryos at one day after fertilization by adding 100
529 µl NaOH and incubating the samples at 95°C for 20 minutes. We then added 10µL Tris-HCl.
530 We performed PCR amplification with the primers listed in Supplementary Table 3, using either
531 'FORD58' or 'FORD60' assays depending on the primer. The thermocycling conditions for the
532 'FORD58' assay were: 95°C for 3 min, followed by 40 cycles of 95°C for 15s, 58°C for 10s,
533 and 72°C for 15s, and a final extension at 72°C for 10 min. The thermocycling conditions for
534 the 'FORD60' assay were: 95°C for 3 min, followed by 40 cycles of 95°C for 15s, 60°C for
535 10s, and 72°C for 15s, and a final extension at 72°C for 10 min. We prepared the PCR amplicons
536 for sequencing using the Nextera XT DNA Library Preparation Kit (Illumina, San Diego, CA,
537 USA) and sequenced them on a MiSeq instrument (Illumina) using 2 X 250 bp cycles (Bek *et*
538 *al.*, 2021). We analyzed the NGS data with CRISPResso2 and determined the mean fraction of
539 reads containing in-frame and out-of-frame indels over different samples, by exporting the
540 allele frequency table, counting the number of reads with both in- and out-of-frame indels or
541 out-of-frame indels only and dividing these numbers by the total number of mapped reads
542 (Fiume *et al.*, 2019). For both the indel and out-of-frame efficiency, the reads with sequencing
543 errors and natural variants were excluded.

544 **RNA extraction and RT-qPCR**

545 The RNA extraction and qPCR protocol described by Bek et al., 2021 was followed,
546 with minor modifications; for each crispant, RNA was extracted from 4 or 5 pools of 10
547 embryos at 7 dpf and 14 dpf using Trizol (Life Technologies Europe) and purified using the
548 RNeasy Mini Kit (Qiagen) with on-column DNase I treatment (Qiagen). RNA concentrations
549 were measured with the Little Lunatic (Unchained Labs) and cDNA was synthesized using the
550 iScript cDNA synthesis kit (Bio-rad). Primers for skeletal marker genes were designed using
551 NCBI Primer-BLAST (Supplementary Table 4) and primers for the housekeeping genes (*elfa*
552 and *bactin2*) were obtained from literature (McCurley & Callard, 2008).

553 The qPCR reaction mixture was prepared with 2.5 µL of SsoAdvanced Universal SYBR
554 Green Supermix (Bio-rad), 5 ng of cDNA, and 250 nM of each primer. The qPCR reaction was
555 run on a LightCycler 480 instrument (Roche) in a white 384-well plate with the following
556 thermocycling conditions: initial denaturation step at 95 °C for 2 min, followed by 44 cycles of
557 denaturation at 95 °C for 5 sec, annealing at 60 °C for 30 sec, and extension at 72 °C for 1 sec.
558 Subsequently, a melting curve analysis was performed with a denaturation step at 95 °C for 5

559 sec, followed by annealing at 60 °C for 1 min and gradual heating to 95 °C at a ramp-rate of
560 0.11 °C/s. Finally, the product was cooled to 37 °C for 3 min (Vanhauwaert *et al.*, 2014). The
561 data was analyzed using the qBase+ software (Biogazelle).
562

563 **Osteoblast imaging in transgenic *osx:*Kaede larvae.**

564 Ten zebrafish larvae (at 7 dpf and 14 dpf) with the transgenic *osx:Kaede* background
565 were anesthetized using 1x Tricaine. Imaging was performed using the Leica microscope
566 M165FC and mounted camera (DFC450C) operated by LAS V4.3 software (Leica
567 Microsystems, Wetzlar, Germany). Images of 7 dpf larvae were taken from the ventral side.
568 Images of 14 dpf larvae were taken from both ventral and lateral perspectives to provide a more
569 comprehensive view of the opercle's surface area.
570 Fiji software (version 2.14.0), powered by ImageJ, was employed for all measurements
571 (Schindelin *et al.*, 2012). Osteoblast-positive area of both the total head and opercle was
572 quantified using thresholding, followed by measurement of the positive area. All measurements
573 were performed in triplicate on blinded pictures. The presence of osteoblasts in the opercle was
574 measured by hand using the polygon selection tool. Mann-Whitney U test was applied in
575 GraphPad Prism (v.9.4.0), with p-values considered significant when ≤0.05.
576

577 **Alizarin red staining and imaging of zebrafish larvae**

578 The ten zebrafish larvae, that were previously used for osteoblast imaging at 7 dpf and
579 14 dpf, were euthanized using 25x Tricaine. They were transferred to a cell strainer and washed
580 with dH2O several times to remove the Tricaine. The strainers were placed in a 6-well plate
581 and incubated in 4% PFA overnight at 4°C. The plates were sealed with parafilm to prevent
582 evaporation. The larvae were then washed with dH2O several times to remove the PFA and
583 bleached for 30 minutes at room temperature using a solution containing 3% H_2O_2 and 2%
584 KOH to remove pigmentation. Next, they were stained overnight at 4°C using Alizarin Red S
585 (0.005% in 1% KOH/2% Triton). The samples were washed with dH2O several times and
586 transferred to increasing concentrations of glycerol (30-70-100% for 5 minutes each) for storage
587 (4°C) and imaging. Zebrafish larvae stained with Alizarin red were then imaged using a Leica
588 M165FC microscope and DFC450C camera with the LAS V4.3 software (Leica Microsystems).
589 The ventral side of the larvae was captured at 7 dpf. Both ventral and lateral perspectives were
590 captured at 14 dpf to provide a more comprehensive view of the opercle's surface area and the
591 number of mineralized vertebrae.

592 Fiji software (version 2.14.0), powered by ImageJ, was employed for all measurements
593 (Schindelin *et al.*, 2012). The red stain in the head elements was assessed using thresholding,
594 followed by quantification of the positive area. These measurements were conducted in
595 triplicate on blinded pictures. The stained notochord tip and opercle was measured by hand
596 using the polygon selection tool. The statistical analysis employed the Mann-Whitney U test in
597 GraphPad Prism (v.9.4.0), with p-values considered significant when ≤0,05.
598

599 **Micro-Computed Tomography (MicroCT) analysis in adult zebrafish**

600 Adult zebrafish (3 months post fertilization) were euthanized using a 25x tricaine
601 solution (4000 mg tricaine powder (Sigma), 979 ml distilled water, and 1M Tris, adjusted to
602 pH 7). Brightfield images of the zebrafish were taken using a Leica M165FC microscope and
603 DFC450C camera with the LAS V4.3 software (Leica Microsystems). The standard lengths of
604 the zebrafish were measured using the Fiji (ImageJ) software (ImageJ 1.52i) (Schindelin *et al.*,
605 2012).
606 The fish were fixed for approximately one week in a fixative solution (4%
607 paraformaldehyde, 5% triton X-100, and 1% potassium hydroxide). The solution was changed
608 when it turned yellow. A maximum of five fish per 100 ml of fixative solution was used. After
609 fixation, the fish were transferred to a 70% ethanol solution for storage until scanning.
610 Before scanning, three fish were transferred to a 15 ml Eppendorf tube and immobilized
611 using paper towel soaked in 70% ethanol. The Eppendorf tubes were scanned at the custom-
612 built HECTOR scanner of the Centre for X-ray Tomography (UGCT, www.ugct.ugent.be). A
613 hardware filter of 0.5 mm Al was used to eliminate beam hardening artefacts, with the tube
614 voltage at 90 kVp and target power of 10 W. During a 360° rotation, 1201 radiographic images
615 were acquired at 1 s acquisition time per image. The raw data was reconstructed using the
616 Octopus Reconstruction software tool, resulting in a 3D volume of approximately
617 2800x1000x1000 voxels. Using geometrical magnification, a voxel size of 20^3 μm^3 was
618 obtained (Masschaele *et al.*, 2013).
619 The 3 fish in one tube were virtually separated from the scan, aligned and exported as 3
620 individual single tiff volume using VGStudioMAX (VolumeGraphics, Heidelberg, Germany).
621 The generated volumes were analyzed using the FishCut software in Matlab described in Hur
622 et al., 2017. The resulting plots were generated using R statistics and were color-coded to
623 highlight significant differences. Significant differences were represented with a lighter color
624 scheme.
625

626 **Alizarin red staining and imaging of adult zebrafish**

627 The fish used for microCT were reused for Alizarin Red staining for which the protocol
628 has been described in Bek et al., 2021. In short, the fish were transferred to cassettes and the
629 concentration of EtOH was gradually reduced from 70% to distilled water (70%-50%-30%-
630 dH2O each 30 min). Then, the samples were enhanced, immersed into the bone-staining
631 medium, stained with bone-staining solution and destained after removal of the scales with
632 destaining solution. Finally, the samples were gradually (30-70-100%) transferred to 100%
633 glycerol for storage (4°C) and imaging.

634 Adult zebrafish were imaged using a Leica M165FC microscope and DFC450C camera
635 with the LAS V4.3 software (Leica Microsystems). The DSR DsRed Dichroic Mirror filter
636 was used to visualize the (red) fluorescent signal. Images were obtained from a lateral view to
637 get a clear picture of the whole fish. Higher magnification was used to get detailed images of
638 the vertebral column and the head. Images of the head were used to measure the head size, using
639 the Fiji (ImageJ) software (Schindelin *et al.*, 2012).

640
641
642
643
644
645
646
647
648
649
650
651
652
653
654
655
656
657

References

Amarasekara, D.S., Kim, S. and Rho, J. (2021), "Regulation of osteoblast differentiation by cytokine networks", *International Journal of Molecular Sciences*, MDPI AG, 2 March, doi: 10.3390/ijms22062851.

Bek, J.W., Shochat, C., De Clercq, A., De Saffel, H., Boel, A., Metz, J., Rodenburg, F., *et al.* (2021), "Lrp5 Mutant and Crispant Zebrafish Faithfully Model Human Osteoporosis, Establishing the Zebrafish as a Platform for CRISPR-Based Functional Screening of Osteoporosis Candidate Genes", *Journal of Bone and Mineral Research*, John Wiley and Sons Inc, Vol. 36 No. 9, pp. 1749–1764, doi: 10.1002/jbmr.4327.

Brent Richards, J., Zheng, H.F. and Spector, T.D. (2012), "Genetics of osteoporosis from genome-wide association studies: Advances and challenges", *Nature Reviews Genetics*, August, doi: 10.1038/nrg3228.

Brett, J.O., Spring, L.M., Bardia, A. and Wander, S.A. (2021), "ESR1 mutation as an emerging clinical biomarker in metastatic hormone receptor-positive breast cancer", *Breast Cancer Research*, BioMed Central Ltd, 1 December, doi: 10.1186/s13058-021-01462-3.

Charoenngam, N., Rittiphairoj, T., Ponvilawan, B., Jaroenlapnopparat, A., Waitayangkoon, P., Suppakitjanusant, P., Prasitsumrit, V., *et al.* (2023), "Bone Fragility in Hereditary Connective Tissue Disorders: A Systematic Review and Meta-Analysis", *Endocrine Practice*, Vol. 29 No. 7, pp. 589–600, doi: https://doi.org/10.1016/j.eprac.2023.02.003.

Clement, K., Rees, H., Canver, M.C., Gehrke, J.M., Farouni, R., Hsu, J.Y., Cole, M.A., *et al.* (2019), "CRISPResso2 provides accurate and rapid genome editing sequence analysis", *Nature Biotechnology*, Nature Publishing Group, 1 March, doi: 10.1038/s41587-019-0032-3.

Concordet, J.P. and Haeussler, M. (2018), "CRISPOR: Intuitive guide selection for CRISPR/Cas9 genome editing experiments and screens", *Nucleic Acids Research*, Oxford University Press, Vol. 46 No. W1, pp. W242–W245, doi: 10.1093/nar/gky354.

Coughlin, C.R., Swanson, M.A., Spector, E., Meeks, N.J.L., Kronquist, K.E., Aslamy, M., Wempe, M.F., *et al.* (2019), "The genotypic spectrum of ALDH7A1 mutations resulting in pyridoxine dependent epilepsy: A common epileptic encephalopathy", *Journal of Inherited Metabolic Disease*, John Wiley and Sons Inc., Vol. 42 No. 2, pp. 353–361, doi: 10.1002/jimd.12045.

Daponte, V., Tonelli, F., Masiero, C., Syx, D., Exbrayat-Héritier, C., Biggiogera, M., Willaert, A., *et al.* (2023), "Cell differentiation and matrix organization are differentially affected during bone formation in osteogenesis imperfecta zebrafish models with different genetic defects impacting collagen type I structure", *Matrix Biology*, Elsevier B.V., Vol. 121, pp. 105–126, doi: 10.1016/j.matbio.2023.06.003.

Dietrich, K., Fiedler, I.A.K., Kurzyukova, A., López-Delgado, A.C., McGowan, L.M., Geurtzen, K., Hammond, C.L., *et al.* (2021), "Skeletal Biology and Disease Modeling in Zebrafish", *Journal of Bone and Mineral Research*, John Wiley and Sons Inc, 1 March, doi: 10.1002/jbmr.4256.

Doench, J.G., Fusi, N., Sullender, M., Hegde, M., Vaimberg, E.W., Donovan, K.F., Smith, I., *et al.* (2016), "Optimized sgRNA design to maximize activity and minimize off-target effects of CRISPR-Cas9", *Nature Biotechnology*, Nature Publishing Group, Vol. 34 No. 2, pp. 184–191, doi: 10.1038/nbt.3437.

El-Brolosy Mohamed A. AND Stainier, D.Y.R. (2017), “Genetic compensation: A phenomenon in search of mechanisms”, *PLOS Genetics*, Public Library of Science, Vol. 13 No. 7, pp. 1–17, doi: 10.1371/journal.pgen.1006780.

Emond, S., Petek, M., Kay, E.J., Heames, B., Devenish, S.R.A., Tokuriki, N. and Hollfelder, F. (2020), “Accessing unexplored regions of sequence space in directed enzyme evolution via insertion/deletion mutagenesis”, *Nature Communications*, Nature Research, Vol. 11 No. 1, doi: 10.1038/s41467-020-17061-3.

Fiume, M., Cupak, M., Keenan, S., Rambla, J., de la Torre, S., Dyke, S.O.M., Brookes, A.J., *et al.* (2019), “Federated discovery and sharing of genomic data using Beacons”, *Nature Biotechnology*, Nature Publishing Group, 1 March, doi: 10.1038/s41587-019-0046-x.

Forlino, A. and Marini, J.C. (2016), “Osteogenesis imperfecta”, *The Lancet*, Lancet Publishing Group, 16 April, doi: 10.1016/S0140-6736(15)00728-X.

Gavaia, P.J., Simes, D.C., Ortiz-Delgado, J.B., Viegas, C.S.B., Pinto, J.P., Kelsh, R.N., Sarasquete, M.C., *et al.* (2006), “Osteocalcin and matrix Gla protein in zebrafish (Danio rerio) and Senegal sole (Solea senegalensis): Comparative gene and protein expression during larval development through adulthood”, *Gene Expression Patterns*, Vol. 6 No. 6, pp. 637–652, doi: 10.1016/j.modgep.2005.11.010.

Gistelinck, C., Kwon, R.Y., Malfait, F., Symoens, S., Harris, M.P., Henke, K., Hawkins, M.B., *et al.* (2018), “Zebrafish type I collagen mutants faithfully recapitulate human type I collagenopathies”, *Proceedings of the National Academy of Sciences of the United States of America*, National Academy of Sciences, Vol. 115 No. 34, pp. E8037–E8046, doi: 10.1073/pnas.1722200115.

Howe, K., Clark, M.D., Torroja, C.F., Torrance, J., Berthelot, C., Muffato, M., Collins, J.E., *et al.* (2013), “The zebrafish reference genome sequence and its relationship to the human genome”, *Nature*, Nature Publishing Group, Vol. 496 No. 7446, pp. 498–503, doi: 10.1038/nature12111.

Hsu, P.D., Scott, D.A., Weinstein, J.A., Ran, F.A., Konermann, S., Agarwala, V., Li, Y., *et al.* (2013), “DNA targeting specificity of RNA-guided Cas9 nucleases”, *Nature Biotechnology*, Vol. 31 No. 9, pp. 827–832, doi: 10.1038/nbt.2647.

Hur, M., Gistelinck, C.A., Huber, P., Lee, J., Thompson, M.H., Monstad-Rios, A.T., Watson, C.J., *et al.* (2017), “MicroCT-based phenomics in the zebrafish skeleton reveals virtues of deep phenotyping in a distributed organ system”, doi: 10.7554/eLife.26014.001.

Jovanovic, M., Guterman-Ram, G. and Marini, J.C. (2022), “Osteogenesis Imperfecta: Mechanisms and Signaling Pathways Connecting Classical and Rare OI Types”, *Endocrine Reviews*, Endocrine Society, 1 February, doi: 10.1210/endrev/bnab017.

Kague, E. and Karasik, D. (2022), “Functional Validation of Osteoporosis Genetic Findings Using Small Fish Models”, *Genes*, MDPI, 1 February, doi: 10.3390/genes13020279.

Kanis, J.A., Melton, L.J., Christiansen, C., Johnston, C.C. and Khaltaev, N. (1994), “The diagnosis of osteoporosis”, *Journal of Bone and Mineral Research*, Vol. 9 No. 8, pp. 1137–1141, doi: 10.1002/jbmr.5650090802.

Kroll, F., Powell, G.T., Ghosh, M., Gestri, G., Antinucci, P., Hearn, T.J., Tunbak, H., *et al.* (2021), “A simple and effective F0 knockout method for rapid screening of behaviour and other complex phenotypes”, *ELife*, Vol. 10, doi: 10.7554/eLife.59683.

Laine, C.M., Joeng, K.S., Campeau, P.M., Kiviranta, R., Tarkkonen, K., Grover, M., Lu, J.T., *et al.* (2013), “WNT1 Mutations in Early-Onset Osteoporosis and Osteogenesis Imperfecta ”, *New England Journal of Medicine*, New England Journal of Medicine (NEJM/MMS), Vol. 368 No. 19, pp. 1809–1816, doi: 10.1056/nejmoa1215458.

Lawrence, C., Best, J., Cockington, J., Henry, E.C., Hurley, S., James, A., Lapointe, C., *et al.* (2016), “The complete and updated ‘rotifer polyculture method’ for rearing first feeding

754 zebrafish", *Journal of Visualized Experiments*, Journal of Visualized Experiments, Vol.
755 2016 No. 107, doi: 10.3791/53629.
756 Li, X., Ominsky, M.S., Niu, Q.T., Sun, N., Daugherty, B., D'Agostin, D., Kurahara, C., *et al.*
757 (2008), "Targeted deletion of the sclerostin gene in mice results in increased bone
758 formation and bone strength", *Journal of Bone and Mineral Research*, Vol. 23 No. 6, pp.
759 860–869, doi: 10.1359/jbmr.080216.
760 Masschaele, B., Dierick, M., Loo, D. Van, Boone, M.N., Brabant, L., Pauwels, E., Cnudde,
761 V., *et al.* (2013), "HECTOR: A 240kV micro-CT setup optimized for research", *Journal*
762 *of Physics: Conference Series*, Vol. 463, Institute of Physics Publishing, doi:
763 10.1088/1742-6596/463/1/012012.
764 McCurley, A.T. and Callard, G. V. (2008), "Characterization of housekeeping genes in
765 zebrafish: Male-female differences and effects of tissue type, developmental stage and
766 chemical treatment", *BMC Molecular Biology*, Vol. 9, doi: 10.1186/1471-2199-9-102.
767 Melville, K.M., Kelly, N.H., Khan, S.A., Schimenti, J.C., Ross, F.P., Main, R.P. and Van Der
768 Meulen, M.C.H. (2014), "Female mice lacking estrogen receptor-alpha in osteoblasts
769 have compromised bone mass and strength", *Journal of Bone and Mineral Research*,
770 Vol. 29 No. 2, pp. 370–379, doi: 10.1002/jbmr.2082.
771 Miton, C.M. and Tokuriki, N. (2023), "Insertions and Deletions (Indels): A Missing Piece of
772 the Protein Engineering Jigsaw", *Biochemistry*, American Chemical Society, 17 January,
773 doi: 10.1021/acs.biochem.2c00188.
774 Morris, J.A., Kemp, J.P., Youlten, S.E., Laurent, L., Logan, J.G., Chai, R.C., Vulpescu, N.A.,
775 *et al.* (2019), "An atlas of genetic influences on osteoporosis in humans and mice",
776 *Nature Genetics*, Nature Publishing Group, Vol. 51 No. 2, pp. 258–266, doi:
777 10.1038/s41588-018-0302-x.
778 Naert, T., Tulkens, D., Edwards, N.A., Carron, M., Shaidani, N.I., Wlizla, M., Boel, A., *et al.*
779 (2020), "Maximizing CRISPR/Cas9 phenotype penetrance applying predictive modeling
780 of editing outcomes in Xenopus and zebrafish embryos", *Scientific Reports*, Nature
781 Research, Vol. 10 No. 1, doi: 10.1038/s41598-020-71412-0.
782 Pouresmaeili, F., Kamalidehghan, B., Kamarehei, M. and Goh, Y.M. (2018), "A
783 comprehensive overview on osteoporosis and its risk factors", *Therapeutics and Clinical*
784 *Risk Management*, Dove Medical Press Ltd., doi: 10.2147/TCRM.S138000.
785 Ralston, S.H. and Uitterlinden, A.G. (2010), "Genetics of osteoporosis", *Endocrine Reviews*,
786 October, doi: 10.1210/er.2009-0044.
787 Rouf, M.A., Wen, L., Mahendra, Y., Wang, J., Zhang, K., Liang, S., Wang, Y., *et al.* (2023),
788 "The recent advances and future perspectives of genetic compensation studies in the
789 zebrafish model", *Genes and Diseases*, KeAi Communications Co., 1 March, doi:
790 10.1016/j.gendis.2021.12.003.
791 Sabik, O.L. and Farber, C.R. (2017), "Using GWAS to identify novel therapeutic targets for
792 osteoporosis", *Translational Research*, Mosby Inc., 1 March, doi:
793 10.1016/j.trsl.2016.10.009.
794 Salhotra, A., Shah, H.N., Levi, B. and Longaker, M.T. (2020), "Mechanisms of bone
795 development and repair", *Nature Reviews Molecular Cell Biology*, Nature Research, 1
796 November, doi: 10.1038/s41580-020-00279-w.
797 Sarmah, S., Barrallo-Gimeno, A., Melville, D.B., Topczewski, J., Solnica-Krezel, L. and
798 Knapik, E.W. (2010), "Sec24D-dependent transport of extracellular matrix proteins is
799 required for zebrafish skeletal morphogenesis", *PLoS ONE*, Vol. 5 No. 4, doi:
800 10.1371/journal.pone.0010367.
801 Savino, S., Desmet, T. and Franceus, J. (2022), "Insertions and deletions in protein evolution
802 and engineering", *Biotechnology Advances*, Elsevier Inc., 1 November, doi:
803 10.1016/j.biotechadv.2022.108010.

Schiavi, J., Fodera, D.M., Brennan, M.A. and McNamara, L.M. (2021), "Estrogen depletion alters osteogenic differentiation and matrix production by osteoblasts in vitro", *Experimental Cell Research*, Elsevier Inc., Vol. 408 No. 1, doi: 10.1016/j.yexcr.2021.112814.

Schindelin, J., Arganda-Carreras, I., Frise, E., Kaynig, V., Longair, M., Pietzsch, T., Preibisch, S., *et al.* (2012), "Fiji: An open-source platform for biological-image analysis", *Nature Methods*, July, doi: 10.1038/nmeth.2019.

Selina, A., Kandagaddala, M., Kumar, V., Abraham, S.S.C., Danda, S. and Madhuri, V. (2023), "SERPINF1 gene variants causing late-onset progressive deforming osteogenesis imperfecta – A study of 18 patients from India", *Bone Reports*, Elsevier Inc., Vol. 18, doi: 10.1016/j.bonr.2023.101690.

Sollis, E., Mosaku, A., Abid, A., Buniello, A., Cerezo, M., Gil, L., Groza, T., *et al.* (2023), "The NHGRI-EBI GWAS Catalog: knowledgebase and deposition resource", *Nucleic Acids Research*, Oxford University Press, Vol. 51 No. 1 D, pp. D977–D985, doi: 10.1093/nar/gkac1010.

Uribe-Salazar, J.M., Kaya, G., Sekar, A., Weyenberg, K.C., Ingamells, C. and Dennis, M.Y. (2022), "Evaluation of CRISPR gene-editing tools in zebrafish", *BMC Genomics*, BioMed Central Ltd, Vol. 23 No. 1, doi: 10.1186/s12864-021-08238-1.

Valenti, M.T., Marchetto, G., Mottes, M. and Dalle Carbonare, L. (2020), "Zebrafish: A Suitable Tool for the Study of Cell Signaling in Bone", *Cells*, NLM (Medline), 17 August, doi: 10.3390/cells9081911.

Vanhauwaert, S., Van Peer, G., Rihani, A., Janssens, E., Rondou, P., Lefever, S., De Paepe, A., *et al.* (2014), "Expressed repeat elements improve RT-qPCR normalization across a wide range of zebrafish gene expression studies", *PLoS ONE*, Public Library of Science, Vol. 9 No. 10, doi: 10.1371/journal.pone.0109091.

Watson, C.J., Monstad-Rios, A.T., Bhimani, R.M., Gistelinck, C., Willaert, A., Coucke, P., Hsu, Y.H., *et al.* (2020), "Phenomics-Based Quantification of CRISPR-Induced Mosaicism in Zebrafish", *Cell Systems*, Cell Press, Vol. 10 No. 3, pp. 275-286.e5, doi: 10.1016/j.cels.2020.02.007.

Westerfield, M. (2000), *The Zebrafish Book: A Guide for the Laboratory Use of Zebrafish (Danio Rerio)*, University of Oregon Press.

Wu, R.S., Lam, I.I., Clay, H., Duong, D.N., Deo, R.C. and Coughlin, S.R. (2018), "A Rapid Method for Directed Gene Knockout for Screening in G0 Zebrafish", *Developmental Cell*, Cell Press, Vol. 46 No. 1, pp. 112-125.e4, doi: 10.1016/j.devcel.2018.06.003.

Zhu, X., Bai, W. and Zheng, H. (2021), "Twelve years of GWAS discoveries for osteoporosis and related traits: advances, challenges and applications", *Bone Research*, Springer Nature, 1 December, doi: 10.1038/s41413-021-00143-3.

850 **Figures**

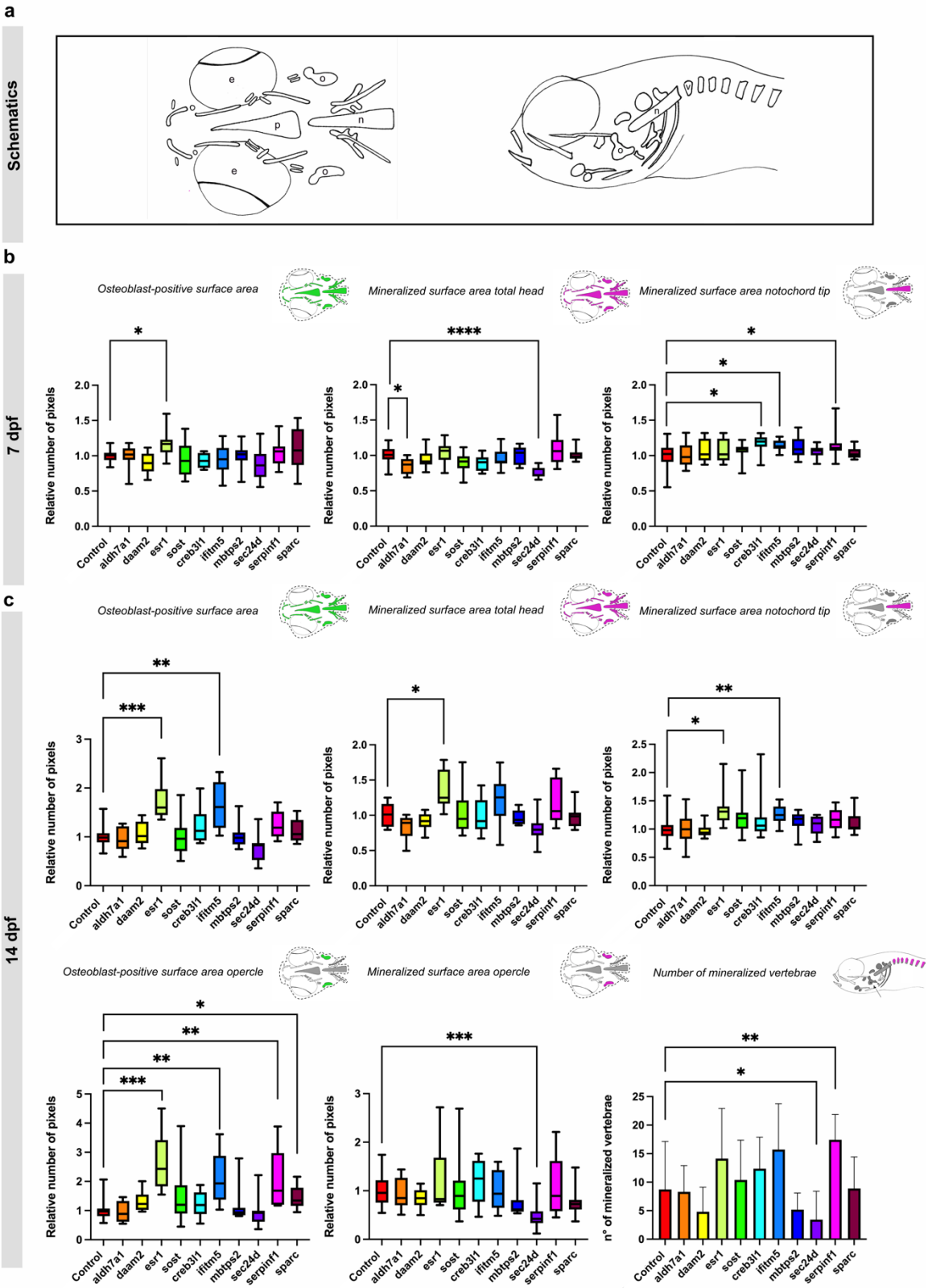

851

Figure 1: Measurements of osteoblast-positive surface area and mineralized surface area of the head skeleton in 7 and 14 dpf crispants. The first four genes are associated with the pathogenesis of osteoporosis, while the last six are linked to osteogenesis imperfecta.(a) Schematic overview of the ventral and lateral perspective of the head of zebrafish larvae at 7 and 14 dpf. The surface area of the total head is circled with a dashed line. Arrows point to the notochord tip (n), the opercle (o) and the mineralized vertebrae. The eyes (e) and parasphenoid (p) are also shown. (b) Quantification of the osteoblast-positive surface area of the total head and the mineralized surface area of the total head and notochord tip at 7 dpf in comparison with their respective controls. (c) Quantification of the osteoblast-positive surface area of the total head and the mineralized surface area of the total head, opercle and notochord tip and number of vertebrae at 14 dpf in comparison with their respective controls. For easier visualization, obtained results were normalized to the respective controls (normalization = individual value crispant (or control) / mean control) (n=10). Statistical significance is evaluated using the Mann-Whitney U -test on non-normalized data and significant differences were visualized using an asterix (= $p \leq 0,05$; ** = $p \leq 0,01$; *** = $p \leq 0,001$; **** = $p \leq 0,0001$). Error bars show the standard deviation of non-normalized data.*

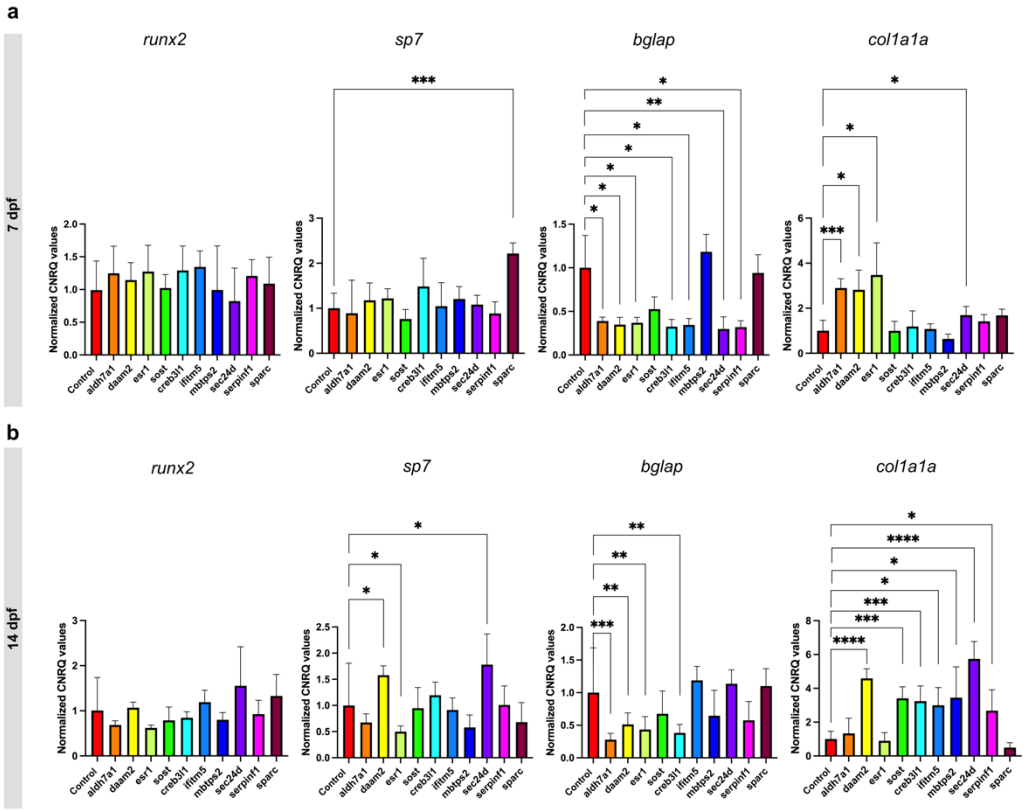

Figure 2: RT-qPCR expression analysis of runx2, sp7, bglap and col1a1a in crispants at 7 (a) and 14 dpf (b) and their respective controls, normalized according to the controls (normalization = individual values crispant (or control) / mean control). The first four genes are associated with the pathogenesis of osteoporosis, while the last six are linked to osteogenesis imperfecta. Statistical significance is evaluated using the Mann-Whitney U test on non-normalized data and significant differences were visualized using an asterix (= $p \leq 0{,}05$; ** = $p \leq 0{,}01$; *** = $p \leq 0{,}001$; **** = $p \leq 0{,}0001$). Error bars show the standard deviation of non-normalized data.*

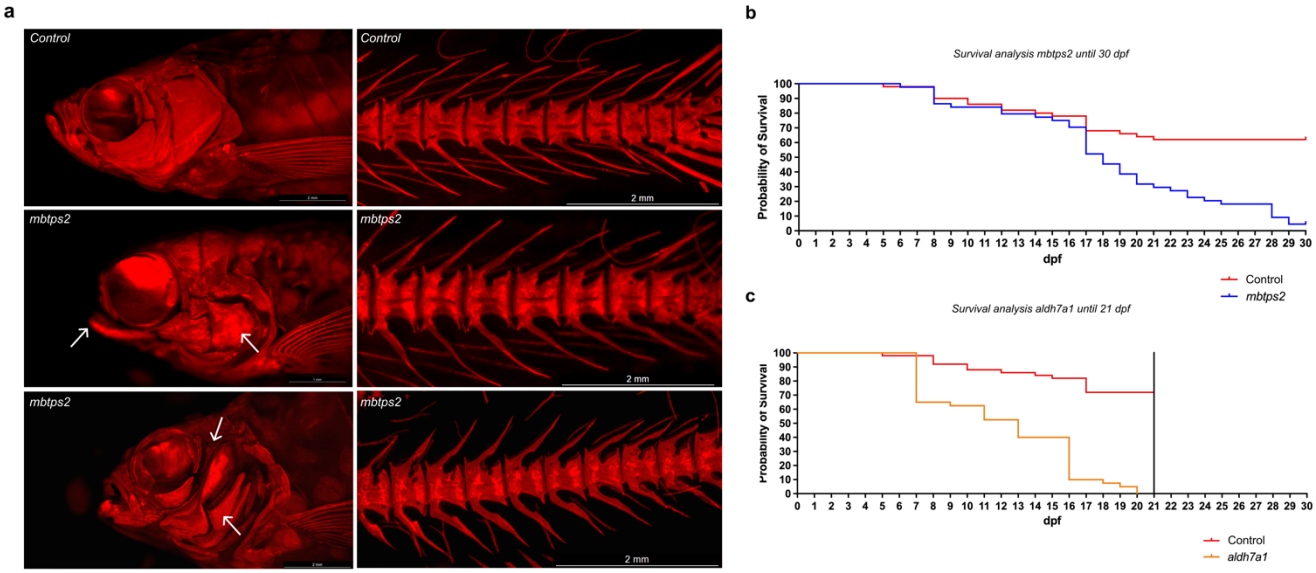

Figure 3: ARS images and survival analysis of mbtps2 crispants. (a) ARS images of control fish and crispants for mbtps2, showing severe craniofacial abnormalities (arrows). (b) Survival curve of controls and crispants for mbtps2, showing a reduction in survival starting from 17 dpf. (c) Survival curve of controls and crispants for aldh7a1, showing a reduction in survival starting from 7 dpf.

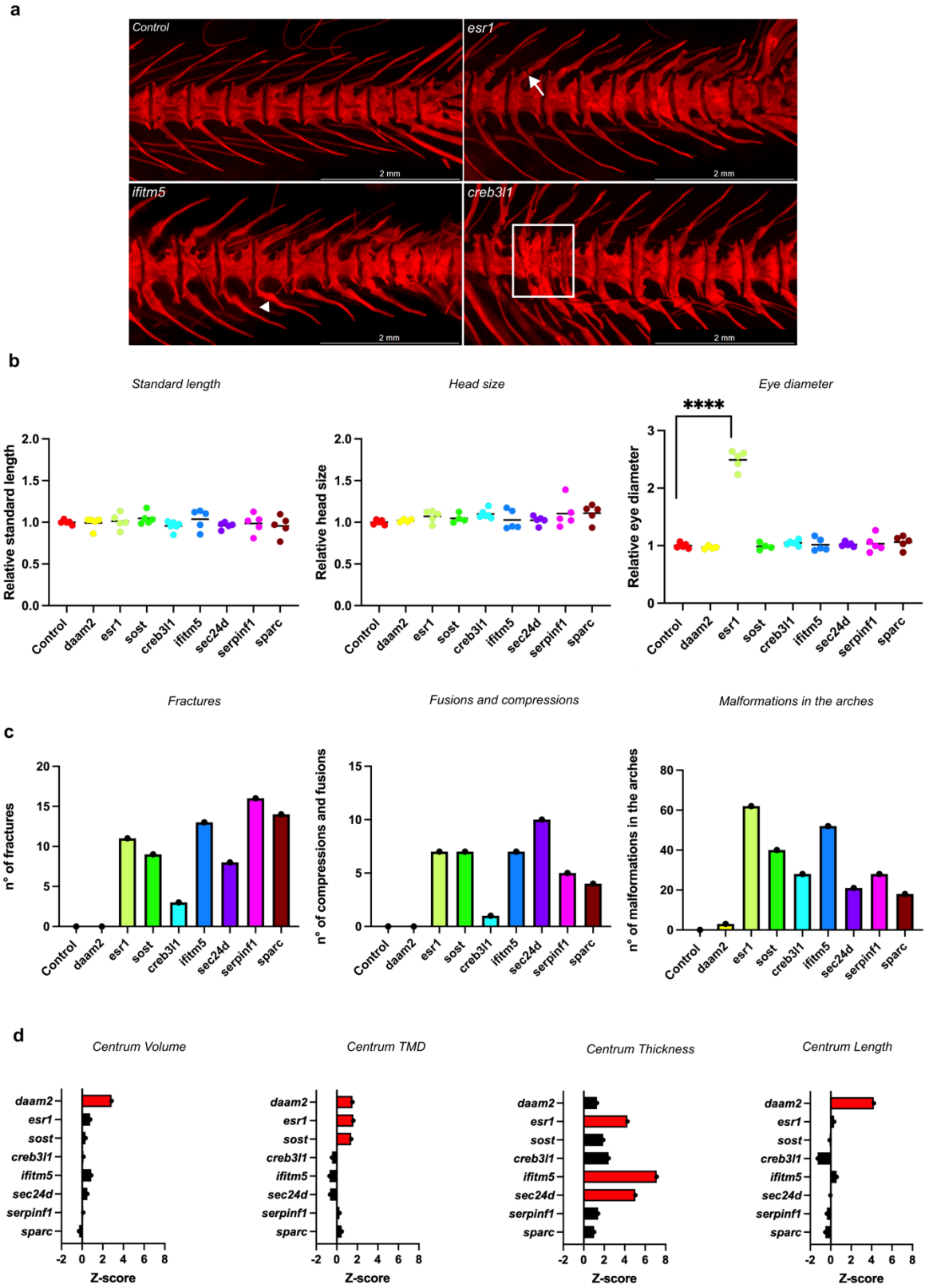

Figure 4: Skeletal phenotyping of adult crispants and their respective controls. The first three genes are associated with the pathogenesis of osteoporosis, while the last five are linked to osteogenesis imperfecta (a) Pictures of ARS-stained vertebral column of a control and three crispants (from left to right: esr1, ifitm5 and creb3l1), showing fractures (arrow), fusions and compressions (squared) and malformations in the arches (arrowhead). (b)

Measurements of the standard length, the head size and the eye diameter of the crispants compared to their control. The standard length was measured from the snout tip to the tail base. The head size was measured from the snout tip to the supraoccipital bone and the eye diameter was measured from the lateral ethmoid to the hyomandibula. The data was normalized for easier visualization (normalization = individual value crispants (or controls) / mean control) (n=5)). (c) Quantification of the number of fractures, fusions or compressions and malformations in the arches of crispants and the controls. For this quantification, twelve vertebrae were selected per fish and a total of 5 crispants per assay was evaluated. Statistical analysis was evaluated using the Mann-Whitney U -test on non-normalized data and significant differences were visualized using an asterix (= $p \leq 0,05$; ** = $p \leq 0,01$; *** = $p \leq 0,001$; **** = $p \leq 0,0001$). Error bars showed the standard deviation of non-normalized data. (d) Quantification of skeletal parameters by quantitative micro-computed tomography (μCT) analysis. In the graphical representation, the different crispants were listed. Statistically significant differences from the control values for a given crispant were depicted as red bars. Significance levels were determined through the global test analysis (Supplementary Figure 7).*

943 # Tables

	aldh7a1	*daam2*	*esr1*	*sost*	*creb3l1*	*ifitm5*	*mbtps2*	*sec24d*	*serpinf1*	*sparc*
% reads with indel	87%	96%	92%	80%	71%	90%	94%	85%	92%	92%
% reads with out-of-frame indel	66%	57%	64%	64%	49%	73%	73%	63%	55%	72%
% reads with in frame indel ≥ 6-bp	16%	24%	15%	14%	11%	15%	19%	12%	25%	16%
% reads likely affecting protein function	82%	81%	79%	78%	60%	88%	92%	75%	80%	88%

944

945 *Table 1: InDelphi-mESC prediction, indel, out-of-frame indel and in-frame rates for the different crispants,*
946 *determined by NGS from pools of 1dpf embryos. The first four genes are associated with the pathogenesis of*
947 *osteoporosis, while the last six are linked to osteogenesis imperfecta. The percentage of reads likely to affect the*
948 *protein function is calculated based on the percentage of reads with out-of-frame indels combined with the*
949 *percentage of reads with in-frame deletions of equal to or more than 6 basepairs.*

950

	aldh7a1	*daam2*	*esr1*	*sost*	*creb3l1*	*ifitm5*	*mbtps2*	*sec24d*	*serpinf1*	*sparc*
Osteoblast-positive surface area total head										
7 dpf	ns	ns	(+)*	ns	ns	ns	ns	ns	ns	ns
14 dpf	ns	ns	(+)***	ns	ns	(+)**	ns	ns	ns	ns
Osteoblast-positive surface area operculum 14 dpf	ns	ns	(+)***	ns	ns	(+)**	ns	ns	(+)**	(+)*
Mineralized surface area total head										
7 dpf	(-)*	ns	ns	ns	ns	ns	ns	(-)****	ns	ns
14 dpf	(-)*	ns	ns	ns	ns	ns	ns	ns	ns	ns
Mineralized surface area notochord tip										
7 dpf	ns	ns	ns	ns	(+)*	(+)*	ns	(+)*	ns	ns
14 dpf	ns	ns	(+)**	ns	ns	(+)*	ns	ns	ns	ns
Mineralized surface area operculum 14 dpf	ns	ns	ns	ns	ns	ns	ns	(-)**	ns	ns
Number of mineralized vertebrae 14 dpf	ns	ns	ns	ns	ns	ns	ns	(-)**	ns	ns
runx2 expression										
7 dpf	ns	ns	ns	ns	ns	ns	ns	ns	ns	ns
14 dpf	ns	ns	ns	ns	ns	ns	ns	ns	ns	ns
sp7 expression										
7 dpf	ns	ns	ns	ns	ns	ns	ns	ns	ns	(+)***
14 dpf	ns	(+)*	(-)*	ns	ns	ns	ns	(+)*	ns	ns
bglap expression										
7 dpf	(-)*	(-)*	(-)*	ns	(-)*	(-)*	ns	(-)**	(-)*	ns
14 dpf	(-)***	(-)**	(-)**	ns	(-)**	ns	ns	ns	ns	ns
col1a1a expression										
7 dpf	(+)***	(+)*	(+)*	ns	ns	ns	ns	(+)*	ns	ns
14 dpf	ns	(+)****	ns	(+)***	(+)***	(+)*	(+)**	(+)****	(+)*	ns
Standard length 90 dpf		ns	ns	ns	ns	ns		ns	ns	ns
Head size 90 dpf		ns	ns	ns	ns	ns		ns	ns	ns
Diameter eye 90 dpf		ns	ns	ns	ns	ns		ns	ns	ns
Centrum Volume 90 dpf		(+)*	ns	ns	ns	ns		ns	ns	ns
Centrum TMD 90 dpf		(+)*	(+)*	(+)*	ns	ns		ns	ns	ns
Centrum Thickness 90 dpf		ns	(+)*	ns	ns	(+)*		(+)*	ns	ns
Centrum Length 90 dpf		(+)*	ns	ns	ns	ns		ns	ns	ns

951

952

953 *Table 2: Overview of the different measurements in crispants at 7, 14 and 90 dpf. The first four genes are*
954 *associated with the pathogenesis of osteoporosis, while the last six are linked to osteogenesis imperfecta. (-):*
955 *downregulation or less, (+) upregulation or more, ns: not significant, asterix defines statistical significance*
956 *(* = $p \leq 0{,}05$; ** = $p \leq 0{,}01$; *** = $p \leq 0{,}001$; **** = $p \leq 0{,}0001$).*

957